ChemPubSoc Europe

DOI: 10.1002/chem.201304795

CHEMISTRY A European Journal Full Paper

Heterogeneous Catalysis

From the Lindlar Catalyst to Supported Ligand-Modified Palladium Nanoparticles: Selectivity Patterns and Accessibility Constraints in the Continuous-Flow Three-Phase Hydrogenation of Acetylenic Compounds

Gianvito Vilé,[a] Neyvis Almora-Barrios,[b] Sharon Mitchell,[a] Núria López,*[b] and Javier Pérez-Ramírez*[a]

Abstract: Site modification and isolation through selective poisoning comprise an effective strategy to enhance the selectivity of palladium catalysts in the partial hydrogenation of triple bonds in acetylenic compounds. The recent emergence of supported hybrid materials matching the stereo- and chemoselectivity of the classical Lindlar catalyst holds promise to revolutionize palladium-catalyzed hydrogenations, and will benefit from an in-depth understanding of these new materials. In this work, we compare the performance of bare, lead-poisoned, and ligand-modified palladium catalysts in the hydrogenation of diverse alkynes. Catalytic tests, conducted in a continuous-flow three-phase reactor, coupled with theoretical calculations and characterization methods, enable elucidation of the structural origins of the observed selectivity patterns. Distinctions in the catalytic performance are correlated with the relative accessibility of the active site to the organic substrate, and with the adsorption configuration and strength, depending on the ensemble size and surface potentials. This explains the role of the ligand in the colloidally prepared catalysts in promoting superior performance in the hydrogenation of terminal and internal alkynes, and short-chain alkynols. In contrast, the greater accessibility of the active surface of the Pd–Pb alloy and the absence of polar groups are shown to be favorable in the conversion of alkynes containing long aliphatic chains and/or ketone groups. These findings provide detailed insights for the advanced design of supported nanostructured catalysts.

Introduction

The partial hydrogenation of acetylenic compounds in the liquid phase is a crucial step in the synthesis of *Z* alkenes, which are indispensable building blocks in the manufacture of polymers, vitamins, fragrances, and agrochemicals.[1] This family of reactions is almost universally carried out over heterogeneous palladium-based catalysts.[2] Major challenges in the Pd-catalyzed partial hydrogenation of alkynes are to prevent the over-hydrogenation of alkenes to the corresponding alkanes and/or the oligomerization of unsaturated moieties. Some degree of control can be achieved by adjustment of the reaction conditions, but the effectiveness is substrate specific, requiring individual tuning.[3] A more common approach to maximize the alkene selectivity involves the modification of palladium by the addition of promoters.[4–13] The Lindlar catalyst (5 wt.% palladium deposited on calcium carbonate or barium sulfate and treated with various forms of lead, yielding a total weight Pd/Pb ratio of 1.5),[14] is the prototypic example of modified Pd catalysts. The widespread use of the Lindlar catalyst for over more than six decades derives from its unique ability to stereo- and chemoselectively transform C≡C into C=C bonds with a predominantly *cis* configuration under mild reaction conditions. Density functional theory (DFT) calculations offered a solid understanding of the selectivity of the Lindlar catalyst,[15] unraveling the role of Pd in alkyne adsorption, H_2 splitting, and H addition, the positive poisoning of Pb in reducing hydride formation, and the function of quinoline, generally added to the reaction mixture, in preventing oligomerization by isolating the adsorption sites. At the present time, economic considerations associated with the high palladium loading and stringent environmental regulations regarding the use of lead provide incentives to seek alternatives to the Lindlar catalyst for alkyne hydrogenations.

Many catalytic systems have been developed in the last decade, such as: 1) Pd nanoparticles prepared with novel deposition techniques;[16–20] 2) Pd-containing bimetallic alloys;[9,13] and 3) catalysts based on alternative active phases.[21–26] In relation to the preparation strategies, colloidal approaches have

[a] G. Vilé, Dr. S. Mitchell, Prof. J. Pérez-Ramírez
Institute for Chemical and Bioengineering
Department of Chemistry and Applied Biosciences, ETH Zurich
Vladimir-Prelog-Weg 1, 8093 Zurich (Switzerland)
E-mail: jpr@chem.ethz.ch

[b] Dr. N. Almora-Barrios, Prof. N. López
Institute of Chemical Research of Catalonia, ICIQ
Av. Països Catalans 16, 43007 Tarragona (Spain)
E-mail: nlopez@iciq.es

Supporting information for this article is available on the WWW under http://dx.doi.org/10.1002/chem.201304795.

proven to be the most versatile tool for synthesizing unsupported nanoparticles with tailored size and shape.[27–34] These materials are prepared from colloidal suspensions of metal nanoparticles and exploit both reducing (i.e., hydrazine or $NaBH_4$) and stabilizing (i.e., surfactants, ionic liquids, polymers, or dendrimers) agents as ligands.[27] Industrially, the use of unsupported Pd nanoparticles prepared through colloidal routes is typically hampered by the use of volatile, toxic, and expensive organic reagents,[35] the absence of a carrier limiting their application as heterogeneous catalysts, and the need for expensive separation techniques (i.e., centrifugation).

Recently, a novel platform of supported ligand-modified palladium catalysts (0.5 wt.% palladium supported on activated carbons or titanium silicate; NanoSelect™) has been developed by BASF and is now commercialized.[35] The catalysts are prepared by using the non-toxic and water-soluble hexadecyl-2-hydroxyethyl-dimethyl ammonium dihydrogen phosphate ($C_{20}H_{44}NO_5P$, HHDMA) ligand, which elegantly integrates both reducing and stabilizing functions in a single molecule (Figure 1). The intrinsic stereo- and chemoselectivity of these materials have been demonstrated in the hydrogenation of selected alkynes and alkynols,[35,36] and the results are consistent with earlier findings on supported Pd catalysts stabilized by polyvinylpyrrolidone (PVP).[37] However, a systematic evaluation of the hydrogenation performance of the NanoSelect™ catalysts, tackling a wider library of acetylenic compounds, investigating kinetic fingerprints, and leading to an improved understanding of the role of HHDMA are of foremost importance to rationalize their selective behavior. Besides, a comparison of the operation mode of NanoSelect™-type catalysts with Lindlar-type catalysts is of great fundamental relevance.

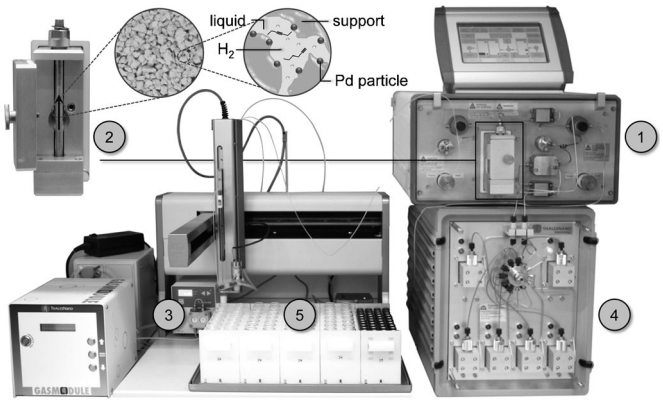

Figure 2. Setup for the evaluation of catalysts in three-phase hydrogenation. The main unit (1) is equipped with an isothermal micro-reactor (zoomed in (2)), pressure and flow controllers, and an electrolytic cell for in situ H_2 generation. The liquid reactant is fed by an HPLC pump (3). The CatChanger™ (4), which consists of six additional isothermal microreactors, enables high-throughput testing and kinetic studies. The XYZ autosampler (5) allows reactant feeding and product collection.

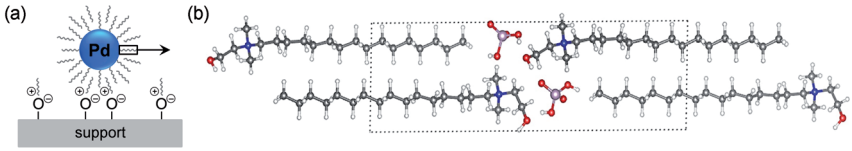

Figure 1. Representation of the NanoSelect™ catalyst (adapted from Ref. [36]) (a) and molecular structure of crystalline hexadecyl(2-hydroxyethyl)dimethylammonium dihydrogen phosphate (HHDMA) determined by DFT calculations (b). The dashed line represents the cell used for the calculations. Color codes: P in pink, O in red, N in dark blue, C in grey, and H in white. The crystallographic information file is provided in the Supporting Information.

Revisiting the development of catalytic materials for alkyne hydrogenation, this work compares the selectivity of bare and alloyed Pd-based catalysts with emerging HHDMA-modified materials prepared by colloidal routes. In view of the obvious benefits in moving from batch- to continuous-mode operation,[38] the hydrogenation performances of terminal or internal alkynes, short- and long-chain alkynols, and acetylenic species containing ketonic groups are evaluated in a continuous-flow reactor (Figure 2). To rationalize the catalytic results, we have carried out density functional theory (DFT) calculations and classical molecular dynamics (MD) simulations, investigating the atomic structure of the NanoSelect™ catalysts and deriving selectivity descriptors, which can be generalized to other ligand-modified palladium catalysts. These results lead to an improved understanding of the performance of colloidal nanoparticles in alkyne hydrogenation, opening new pathways for the design of highly selective catalysts with tailored properties.

Results and Discussion

Characterization of the Pd-based catalysts

Four supported palladium catalysts (bare Pd/Al_2O_3, Lindlar-like $Pd\text{-}Pb/CaCO_3$, and the two ligand-modified c-Pd/C and c-Pd/TiS) are characterized by multiple techniques in order to establish the relative loading and dispersion of palladium, the morphology and porosity of the support, and the content and thermal stability of organic molecules adsorbed on the ligand-modified materials.

The Pd/Al_2O_3 catalyst has been characterized extensively in prior works.[6,39] The material contains approximately 1 wt.% Pd (Table 1); uniformly sized palladium nanoparticles of about 4 nm average diameter (Figure S1a in the Supporting Information) decorate the Al_2O_3 support. The catalyst exhibits a Brunauer–Emmett–Teller (BET) surface area of 181 $m^2 g^{-1}$ and a pore volume of 0.90 $cm^3 g^{-1}$ (Table 1). Comparatively, the Lindlar catalyst contains 4.53 wt.% Pd and, in addition, 3.41 wt.% Pb. The surface atomic Pd/Pb ratio, determined by XPS, is about 1.3, in agreement with early reports.[40] Microscopic examination reveals that the Pd–Pb nanoparticles are well-distributed over the support (Figure S1b), but are significantly larger (ca. 14 nm in diameter) than in the case of Pd/Al_2O_3. This is expected considering that the Lindlar catalyst contains a five times higher palladium loading. The available BET surface area is limited (10 $m^2 g^{-1}$), because the basic $CaCO_3$ support is composed of large, nonporous particles ($V_{pore} = 0.03$ $cm^3 g^{-1}$). Particularly, the

Table 1. Characterization data of the palladium catalysts.

Catalyst	Pd[a] [wt.%]	Pb[a] [wt.%]	N[b] [wt.%]	S_{BET}[c] [$m^2 g^{-1}$]	V_{pore}[d] [$cm^{-3} g^{-1}$]	D[e] [%]
Pd/Al_2O_3	1.00	-	–	181	0.90	22
$Pd\text{-}Pb/CaCO_3$	4.53	3.41	–	10	0.03	6
c-Pd/C	0.56	–	0.72	336	0.41	12
c-Pd/TiS	0.52 (0.51)[f]	–	0.49 (0.02)[f]	231 (137)[f]	0.16 (0.12)[f]	14 (17)[f]

[a] ICP-OES. [b] Elemental analysis. [c] BET method. [d] Volume adsorbed at $p/p_0 = 0.99$. [e] CO pulse chemisorption. [f] After UV–ozone treatment for 120 min between brackets.

absence of microporosity for the Pd/Al_2O_3 and Lindlar catalysts is beneficial in order to avoid diffusion limitations.

The catalysts prepared by colloidal routes (c-Pd/C and c-Pd/TiS) contain about 0.5 wt.%. Examination of the catalysts by high-angle annular dark-field scanning transmission electron (HAADF-STEM) and SEM (Figure 3a and b) reveals that the supported nanoparticles possess a uniform, spherical shape, exhibiting average diameters of around 6 and 7 nm for c-Pd/C and c-Pd/TiS, respectively. Despite distinctions in the morphology and porosity of the activated carbons and titanium silicate supports, the nanoparticles appear discretely dispersed over the external surface of both materials. These findings confirm the observation of a previous study on the metal distribution in c-Pd/C, which suggested that the greater surface area of the activated carbon support ($S_{BET} = 336\ m^2 g^{-1}$, Table 1) is hardly utilized since an egg-shell distribution of palladium on the support is obtained.[36] The denser arrangement of nanoparticles in the case of c-Pd/TiS can be ascribed to the larger particle size of the support, although the BET surface area of the sample ($S_{BET} = 231\ m^2 g^{-1}$) is relatively high. The microporosity of the c-Pd/C catalyst ($V_{micro} = 0.03\ cm^3 g^{-1}$) is also confirmed by the higher uptake of N_2 at low relative pressures (Figure S2 in the Supporting Information). The degree of Pd dispersion calculated from the microscopy-derived particle size distributions (19% for c-Pd/C and 16% for c-Pd/TiS) is slightly higher than that determined by CO chemisorption (12% and 14%, respectively), indicating that some of the palladium atoms are inaccessible. XPS measurements (Figure S3 in the Supporting Information) evidence a single peak for the Pd $3d_{5/2}$ core level (at 335.0 eV for c-Pd/C and 335.3 eV for c-Pd/TiS) corresponding to Pd^0,[41] which indicates that the surface of the Pd nanoparticles is entirely reduced.

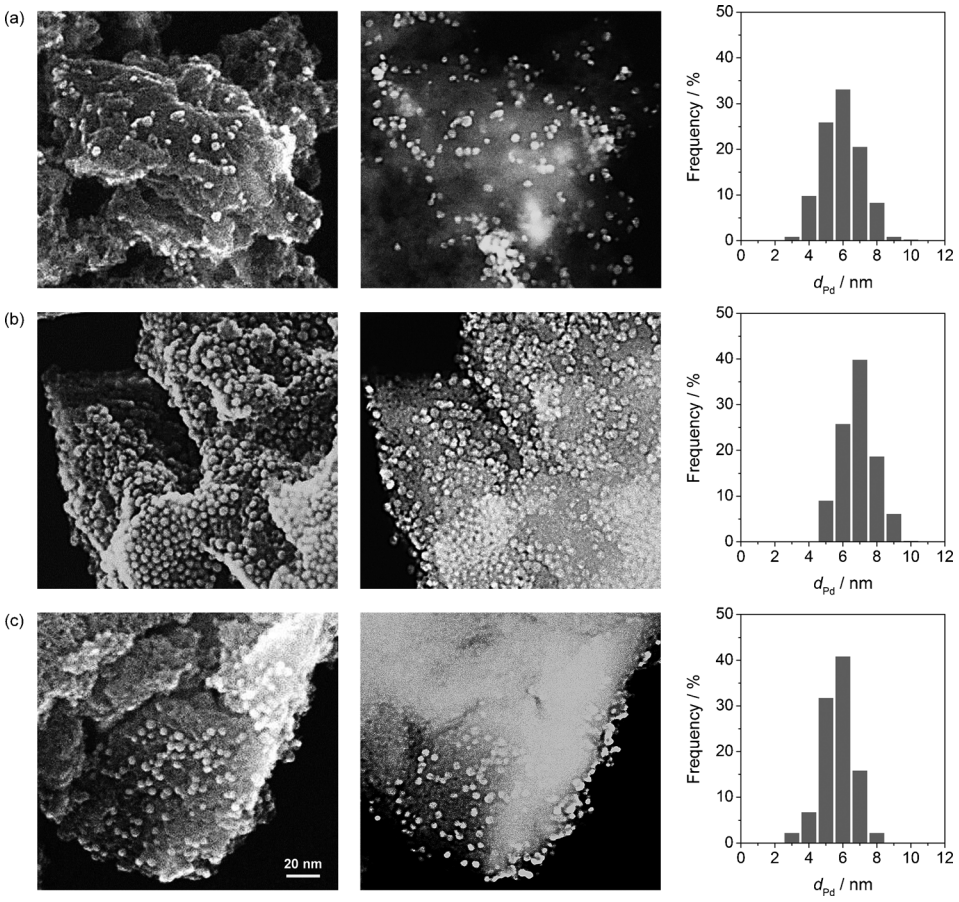

Figure 3. SEM (left) and HAADF-STEM (middle) micrographs and respective particle size distributions of palladium of c-Pd/C (a), c-Pd/TiS (b), and c-Pd/TiS after UV–ozone treatment for 120 min (c). The 20 nm scale bar applies to all micrographs.

The presence of HHDMA molecules on the surface of the c-Pd catalysts is confirmed by the observation of pronounced bands between 3000 and 2800 cm^{-1} in the infrared spectra of the samples (Figure 4a).[42,43] Despite the similar preparation protocols,[35] quantitative elemental analysis of N reveals that the residual amounts are higher for c-Pd/C than for c-Pd/TiS. This is associated with an enhanced adsorption of HHDMA on the surface of the activated carbon support,[36] which prevents a reliable estimation of the amount of stabilizer molecules per surface palladium atom. The stability of the HHDMA molecules is compared by thermogravimetric analysis in air (Figure 4b and c). Both samples show a pronounced weight loss at 340 K, associated to the removal of physisorbed water from the support, and a further loss at 570–580 K, which is assigned, based on evolved-gas analysis by mass spectrometry, to the decomposition of the or-

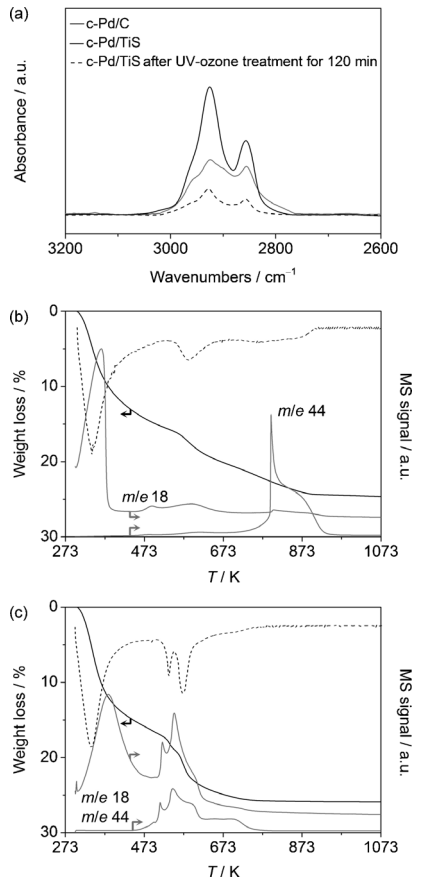

Figure 4. C–H stretching region of the DRIFT spectra recorded in He at 473 K (a). Thermogravimetric profiles in air with the corresponding MS signals of water (*m/e* 18) and carbon dioxide (*m/e* 44) of c-Pd/C (b) and c-Pd/TiS (c). In (a), the reduced absorbance in the near-infrared region of the darker carbon-supported catalyst compared with c-Pd/TiS precludes quantitative analysis in the infrared spectra. In (b) and (c), the dashed line represents the first derivative curve of the thermogravimetric profile.

ganic capping layers. The c-Pd/C catalyst also shows a weight loss at ca. 800 K, associated with the decomposition of the support.[36] In this case, the oxidative decomposition of the support dominates the mass signal measured.

To confirm the impact of the residual HHDMA species on the properties of the supported catalysts, we have applied controlled UV–ozone treatments to remove the organic layer.[30,34] Herein, the simultaneous action of ozone and ultraviolet light oxidizes carbon-containing compounds into carbon dioxide and water. As shown in Figure 4a, the IR spectrum of c-Pd/TiS shows negligible absorbance at 3000–2800 cm^{-1} after UV–ozone treatment for 2 h. This confirms the almost complete removal of the organic layer, as also evidenced by elemental analysis of N (Table 1). Comparison of the SEM/HAADF-STEM micrographs (Figure 3c) demonstrates that the UV–ozone treatment does not significantly alter the size or morphology of the Pd nanoparticles, and the Pd content determined by inductively coupled plasma optical emission spectroscopy (ICP-OES) is unaltered.

Structure of HHDMA-modified Pd

From the characterization data, it appears that the ligand HHDMA covers the surface of the colloidally prepared catalysts. Therefore, dispersion-corrected DFT calculations have been applied in order to attain an atomic understanding of the structure of the c-Pd. So far, this has been impeded by factors such as: 1) the need to account for all interactions including van der Waals forces, which determine the stabilizing contribution of the aliphatic tails; 2) the necessity for unit cells sufficiently large to represent the surfactant structure; and 3) the need to input the crystal structure of the surfactant, which in many cases remains unknown.

The first step involves the definition of an appropriate crystal structure for the HHDMA molecule in the presence of the dihydrogen phosphate anion. Although the lattice of the precursor, $(HHDMA)_2PdCl_4$, has been reported in the literature,[35] this data cannot be directly employed because of the different identity of the anions. Nevertheless, the crystal lattice that we have calculated (Figure 1b) shares common features with the structure of its precursor. In fact, the two aliphatic chains of the HHDMA molecule are arranged linearly by van der Waals interactions. Electrostatic forces hold the quaternary ammonium headgroups of HHDMA in close proximity to the $H_2PO_4^-$ anion, and this interaction is further reinforced by a hydrogen bond between the CH_2OH side tail and the $H_2PO_4^-$ group. The structures yield N–P contacts of 4.225 Å.

The anionic dihydrogen phosphate group strongly adsorbs on the surface of Pd(111),[44] and the long-chain cationic counterion adapts to the configuration of the anion by electrostatic interactions. The adsorption is exothermic by 4.59 eV per HHDMA molecule and the final structure fits naturally in the $p(2\times2)$ supercell without any further restriction. The three oxygen atoms of the phosphate group reside close to the metal sites, with an average Pd–O distance of 2.524 Å, and the cationic headgroups are located 7.593 Å from the Pd surface. Upon adsorption, the $H_2PO_4^-$ species tend to dissociate (Figure S4, Table S1 in the Supporting Information), forming HPO_4^{2-} and H^+ and further releasing 0.29 eV. In this process, the whole ligand moves closer to the surface. In fact, the average Pd–O distance reduces to 2.365 Å, the Pd–N distance is 7.469 Å, and the hydrogen bond between the HPO_4^{2-} anion and the CH_2OH tail is 2.375 Å. As shown in Figure 5 and additionally displayed in Movie 1 (in the Supporting Information), this structure very effectively limits the size of the Pd ensemble, which can be expected to block potential oligomerization pathways. DFT calculations indicate that the enlargement of the ensemble size to accommodate a bulky adsorption configuration by displacement of a hydrogen phosphate on the surface of palladium would incur a large energy penalty (1.19 eV) due to the repulsive interactions between the anionic head groups. The latter ultimately explains the relative inflexibility of the $[H_2PO_4]^-$–Pd layer. On the other hand, classical MD simulations performed in large simulation cells demonstrate that the aliphatic chains of the surfactant are highly mobile, opening pores that are dynamically closed in a nanosecond time frame

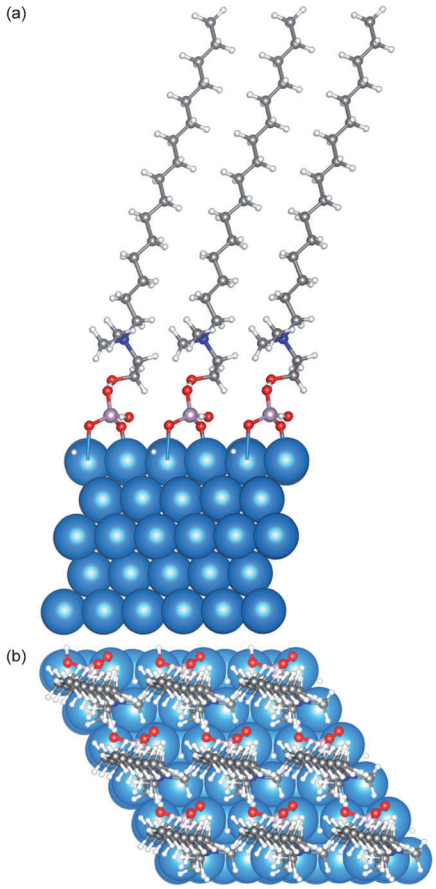

Figure 5. Side (a) and top view (b) of the DFT-calculated adsorption configuration of HHDMA molecules on Pd(111). The configuration of the adsorbed anion is HPO_4^{2-}. The blue spheres represent Pd sites, and the ball and stick models represent the adsorbed HHDMA. The color codes are indicated in Figure 1. A movie file displaying the 3D structure is provided as Supporting Information.

(Figure S5 in the Supporting Information). These pores present elliptical shapes with a maximum diameter of less than 10 Å.

Performance of the Pd-based catalysts

The selective properties of the Pd catalysts were evaluated in the reduction of acetylenic species of varying complexity, under continuous-flow liquid-phase conditions. In contrast to batch and semi-batch setups, commonly employed for laboratory testing, a continuous-flow three-phase reactor can be efficiently operated at steady state, offering several advantages for industrial implementation.[38]

In the hydrogenation of linear, terminal alkynes (1-pentyne and 1-hexyne; respectively, Entry 1 and 2 of Table 2), the non-promoted Pd/Al_2O_3 catalyst is poorly selective to the corresponding olefins (ca. 70%) and yields over-hydrogenated products and oligomers. This is typical of monometallic Pd, which needs modification in order to suppress the formation of hydrides and carbides, thereby stabilizing a high alkene yield. As expected, the Lindlar catalyst shows an excellent degree of selectivity to the terminal olefin (nearly 100%), owing to the presence of lead, which strategically deactivates the palladium sites. Comparatively, the two ligand-modified catalysts (c-Pd/C and c-Pd/TiS) are also intrinsically selective (100%) to the production of terminal olefins. This outstanding degree of selectivity has been confirmed for the solvent-free hydrogenation of 1-hexyne (100% selectivity to 1-hexene at 36% 1-hexyne conversion). Upon application of substrates with an internal triple bond, as for the hydrogenation of 3-hexyne (Entry 3), the materials prepared through colloidal routes yield the *cis*-alkene. This stereoselectivity, matching the performance of conventional Pd-Pb alloys at much lower Pd loadings, is attractive for the pharmaceutical and fine chemical industries.

On the other hand, in the hydrogenation of enynes and alkynols (Entries 4–7), the chemoselectivity patterns observed over the Lindlar and ligand-modified catalysts depend on the substrate. In the hydrogenation of valylene (Entry 4), the colloidal and Lindlar catalysts predominantly yield isoprene, and the selectivity to 3-methyl-1-butyne, obtained by the reduction of the double bond, is only about 5%. 'Bare' palladium, in contrast, produces isoprene, 3-methyl-1-butyne, and other over-hydrogenated products. Similarly, the lowest degree of selectivity in the hydrogenation of 2-methyl-3-butyn-2-ol (Entry 5), 3-methyl-1-pentyn-3-ol (Entry 6), and 3-methyl 1-penten-4-yn-3-ol (Entry 7) is observed over the Pd-only nanoparticles (*S*-(alkenols) = 70, 67, and 58%, respectively). In this case, the Lin-

Table 2. Hydrogenation of acetylenic compounds over palladium catalysts.

Entry	Substrate	Desired product	Selectivity[a] [%] Pd/Al_2O_3	$Pd\text{-}Pb/CaCO_3$	c-Pd/C	c-Pd/TiS
1		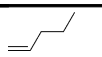	71	98	100	100
2			67	100	97	96
3			53	100	97	100
4			65	92	93	96
5			70	85	100	96
6			67	83	100	97
7			58	76	86	87
8			73	97	85	93
9	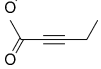	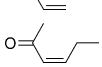	74	83	63	66

[a] Reaction conditions: $T = 293$ K, $P = 1$ bar, $F_G(H_2) = 18\ cm^3\ min^{-1}$, $F_L(\text{substrate} + \text{solvent}) = 0.3\ cm^3\ min^{-1}$. Under these conditions, the degree of alkyne conversion is between 24–35% over all catalysts.

dlar catalyst shows a higher selectivity (85, 83, and 76%, respectively) at the same degree of alkynol conversion; and notably, the colloidally prepared catalysts are fully chemoselective to the alkene, as the OH functionality is not reduced. This excellent result, exceeding those of conventional Pd systems, should be connected with the presence of HHDMA on the surface of Pd (vide infra). However, in the hydrogenation of alkynes containing a ketone group, such as 3-butyn-2-one (Entry 8) and 3-hexyn-2-one (Entry 9), the novel c-Pd catalysts are less selective to 3-buten-2-one and *cis*-3-hexen-2-one than Pd-Pb/$CaCO_3$. Considering that at elevated temperature (333 K) and pressure (8 bar), the ligand-modified materials yield unsaturated alcohols (3-buten-2-ol and *cis*-3-hexen-2-ol) with high selectivity (85%), it can be expected that the ketone group interacts with the surface of Pd and/or with the polar and protic functionalities of HHDMA.

Focusing on the hydrogenation of 1-hexyne, Figure 6a displays the relation between the degree of alkyne conversion and the selectivity to 1-hexene, at 293 K and 1 bar. Over the monometallic Pd/Al_2O_3, the selectivity to 1-hexene decreases with an increasing alkyne conversion. Here, the Lindlar catalyst and c-Pd/TiS preferentially form the olefin (ca. 100%), even at X(1-hexyne) > 90%. The intrinsic selective character of the Lindlar and ligand-modified catalysts over a broad degree of conversion was also confirmed in the hydrogenation of 3-hexyne (Figure 6b), and valylene (Figure 6c). The selectivity to the alkene product over the c-Pd catalysts only drops when higher temperatures (293-353 K) and pressures (1–9 bar) are applied, and the contour plot in Figure 7 highlights the selectivity window for the hydrogenation of 1-hexyne over the ligand-modified catalysts (T < 313 K and P < 2 bar); outside this range, *n*-hexane and 2-hexene are formed.

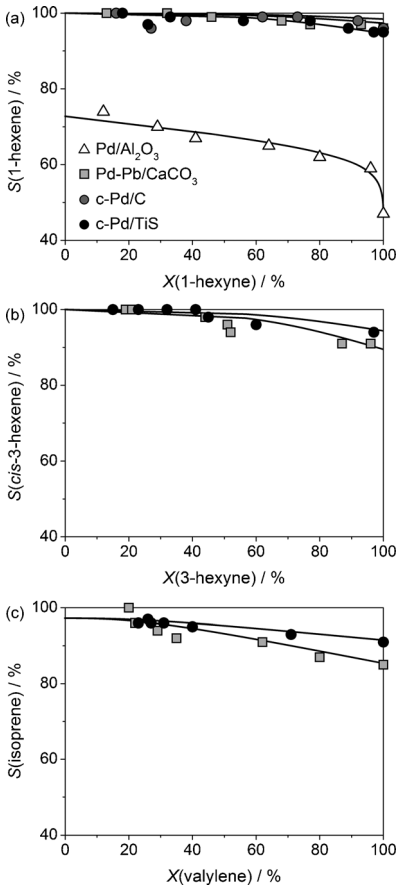

Figure 6. Selectivity to 1-hexene (a), *cis*-3-hexene (b), and isoprene (c) as a function of the conversion of 1-hexyne, 3-hexyne, and valylene over the palladium catalysts. Reaction conditions: T = 293 K, P = 1 bar, $F_G(H_2)$ = 9–60 $cm^3 min^{-1}$, F_L(substrate + solvent) = 0.3–3 $cm^3 min^{-1}$. The data at 100% conversion were collected with double the amount of catalyst.

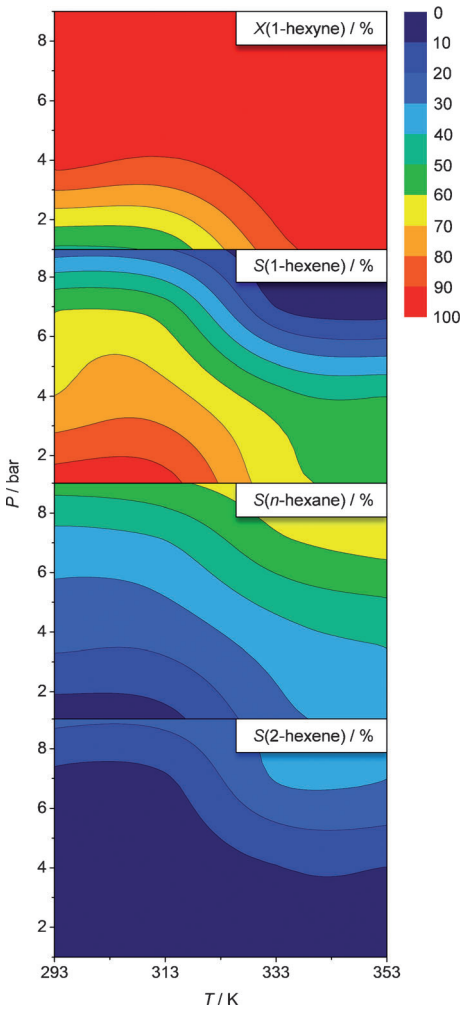

Figure 7. Contour plots of the hydrogenation of 1-hexyne over c-Pd/TiS at different temperatures and pressures. Reaction conditions: $F_G(H_2)$ = 18 $cm^3 min^{-1}$, F_L(substrate + solvent) = 0.3 $cm^3 min^{-1}$.

It should be emphasized that the equivalent selectivity evidenced over the two colloidally prepared Pd catalysts in all of the catalytic tests suggests that the specific influence of the support is minor (Figure S6 in the Supporting Information). This result differs from previous findings, which reported a lower degree of selectivity over c-Pd/C.[36] The contrasting observation could relate to the different mode of operation (batch vs. continuous-flow reactor) adopted in that study.[38]

Molecular-level understanding of the selectivity patterns

In order to rationalize the hydrogenation performance of the catalysts presented in Table 2, DFT calculations using dispersion interactions have been applied. We have considered the adsorption of selected model reactants (specifically, ethyne, ethene, formaldehyde, and methanol) in order to understand the hydrogenation performance observed for the functionalized alkynes in Table 2. The adsorption energies are obtained as: $E_{ads} = E_{cat+mol} - E_{cat} - E_{mol}$, where $E_{cat+mol}$ is the energy of the catalyst with the adsorbed reactant, E_{cat} is the energy of the catalyst (eventually covered by the ligand, HHDMA), and E_{mol} is the energy of the specific reactant. The results are summarized in Figure 8, and the corresponding structures are presented in

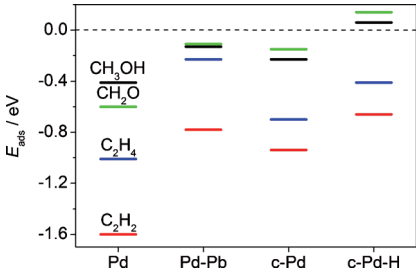

Figure 8. Adsorption energies of ethyne, ethene, formaldehyde, and methanol on the Pd(111), Pb-Pd(111), and c-Pd(111) surfaces. For the c-Pd sample, two different configurations of the adsorbed anion have been employed: $H_2PO_4^-$ (c-Pd) and HPO_4^{2-} (c-Pd-H).

Figure S7 in the Supporting Information. The theoretical results for the alloyed Pd–Zn[9] and Pd–Ga,[25] which are also selective hydrogenation catalysts, parallel those of Pd–Pb (Figure S8 in the Supporting Information). Therefore, for the sake of conciseness, only the latter will be presented here.

Terminal and internal alkynes (1-pentyne, 1-hexyne, and 3-hexyne) are selectively hydrogenated over the Pb-poisoned and ligand-modified Pd catalysts, whereas the monometallic Pd nanoparticles generate alkanes and oligomers. This result can be explained on the basis of the thermodynamic selectivity concept (a selective catalyst offers preferential adsorption of the alkyne and a low stability to the adsorbed alkene).[4,21] The adsorption of ethyne on bare Pd is highly exothermic (1.6 eV), and its hydrogenation produces the vinyl intermediate,[3] which is the precursors for the formation of ethylene. However, once formed, the alkene remains on the catalyst surface, as its adsorption energy is −1.0 eV, and can be over-hydrogenated or oligomerized. On the other hand, the desorption of the alkene from Pb- and HHDMA-'poisoned' surfaces is much less exothermic (0.23 and 0.41 eV, respectively), occurring spontaneously under the conditions studied, which justifies the absence of oligomers over the Lindlar and the colloidally prepared catalysts (Table 2 and Figure 7).

Similarly, β-hydride phases formed by the penetration of hydrogen into the Pd lattice can be explained by the adsorption energy of H atoms on surface and subsurface positions. The average adsorption energy of H on the surface of a clean Pd catalyst is −0.54 eV per H atom, and the differential adsorption energy in the subsurface is thermoneutral. Thus, the adsorption takes place on the whole surface and, when the first layer is completely covered, on subsurface positions. The H species accumulated in the subsurface of palladium are easily transferred to the adsorbed hydrocarbons,[4,6] yielding fully saturated species, in agreement with the results displayed in Table 2, Figure 6, and Figure 7 for Pd/Al_2O_3. For the Pd–Pb system, the exothermic adsorption energy of H on the surface (−0.52 eV) is similar to that of Pd, although less active sites are available. Moreover, the differential adsorption energy for the addition of H layers in the subsurface is endothermic (0.23 eV). Therefore, Pd alloys are less prone to form β-hydrides.[15] Interestingly, the action of the ligand on the catalyst prepared by colloidal routes is similar to that of Pb in the Lindlar catalyst, effectively reducing the number of active sites (geometric effect) and the adsorption energy of H in the first layer (−0.39 eV) (electronic effect). This explains the intrinsic alkene selectivity of the HHDMA-modified catalysts (Table 2 and Figure 6). However, the adsorption of H in the subsurface is only slightly endothermic (0.07 eV). Therefore, if high H_2 pressures are employed, over-hydrogenation reactions cannot be avoided, as observed in Figure 7. The solvent might, to a certain extent, mitigate this problem, since it may reduce the amount of H_2 in contact with the surface. Isomerization of the alkenes takes place through the Horiuti-Polanyi mechanism, depending on the amount of hydrogen that can be stored by the catalyst. As HHDMA-modified catalysts can keep a significant amount of hydrogen at $P > 2$ bar, this explains the experimental formation of 2-hexene seen in Figure 7.

The Lindlar and ligand-modified catalysts are intrinsically stereoselective to *cis* alkenes in the hydrogenation of internal alkynes (Table 2). The stereoselectivity of the hybrid palladium catalysts is related to the small ensembles generated by either Pb alloying or by HHDMA adsorption. This limited ensemble ensures a lower coverage of H on the catalyst surface, preventing the H addition to the C radical and the reorganization/isomerization of the radical species.

The chemoselective hydrogenation of valylene to isoprene occurs primarily due to the adsorption of the triple bond on the surface. Due to the immobility of the phosphate groups discussed earlier and the rigidity of valylene, the ensemble is too small to simultaneously adsorb the double bond. Similarly, in the case of 2-methyl-3-butyn-2-ol, 3-methyl-1-pentyn-3-ol, and 3-methyl-1-pentyn-4-yn-3-ol (Table 2), the higher selectivity observed over the ligand-modified than the bare or alloyed Pd catalysts are related to the interaction of the hydroxyl group with the Pd surface. The adsorption energy of methanol is −0.41 eV on Pd and −0.13 eV on Pd–Pb. As the alkynols investigated also contain unsaturated bonds, these values are further reduced by the contribution of C≡C and C=C bonds. Therefore, the molecules adsorb strongly on the surface (in line with previous studies on the hydrogenation of enynes),[45] further reacting with H species and reducing the process selectivity. This effect is not encountered on the c-Pd catalysts, as the adsorption energy of an alcohol group with the coated surface is slightly endothermic (0.06 eV).

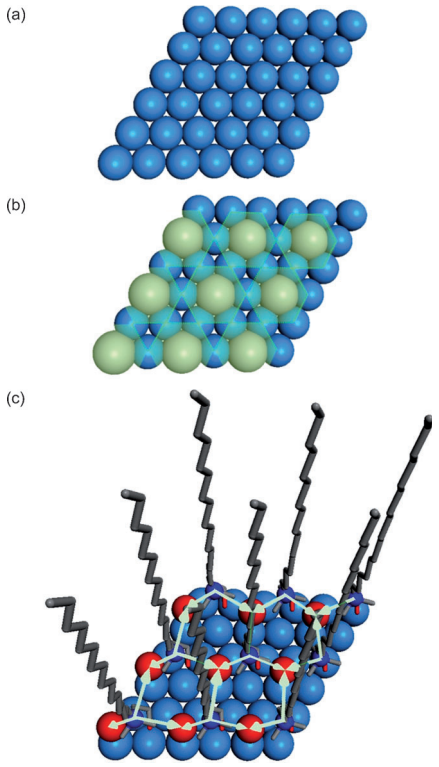

Figure 9. Schematic representation of the surface of Pd (a), Pd-Pb (b), and c-Pd (c). In the Pb-poisoned Pd catalyst (b), the superposition of the Pb exclusion areas is indicated by green hexagons and the available active sites are enclosed by triangular regions. This represents a two-dimensional catalytic surface. In the three-dimensional colloidal-based architecture (c), the electric field generated by the adsorption of HHDMA is represented by green arrows.

Finally, for the hydrogenation of 3-butyn-2-one and 3-hexyn-2-one, the superior performance of the Lindlar catalyst with respect to c-Pd surfaces can be traced back to the protic nature of the c-Pd and the electric fields presented at the surface (Figure 9). The adsorption energy of the carbonyl group is −0.60 and −0.11 eV for Pd–Pb and c-Pd, respectively. As the phosphate anion is protic, it can easily transfer one of the hydrogen atoms to the incoming ketone, establishing further acid–base equilibria where the phosphate group behaves as a buffer for hydrogen atoms. This behavior, resembling somehow that of enzymes and ionic-liquid-stabilized nanoparticles with strong directing electric fields and proton shuttles,[28,32] is not encountered on bare and alloyed Pd and explains the reduction of the ketone group, which impairs the selectivity to the alkenones.

Access and adsorption constraints in hybrid Pd catalysts for alkyne semi-hydrogenation

Most of the alkynes employed in the pharmaceutical and fine chemical industries comprise long-chained, highly branched compounds containing an internal triple bond and additional functionalities. Stereo- and chemoselective hydrogenation only occurs if the C≡C unsaturation can be adsorbed on the palladium site. However, for c-Pd, the presence of the ligand imposes severe access and/or adsorption constraints, which are controlled by the chemical and physical nature of the HHDMA layer. To unravel the effects of these limitations, the performances of the Lindlar and NanoSelect™ catalysts have been evaluated in the hydrogenation of acetylenes of varying adsorption length. Particularly, the adsorption length has been obtained from the density isocontour[46] and is defined as the size of the hydrocarbon when the triple bond is activated on palladium. In fact, as shown in Figure S9 in the Supporting Information, this length differs from that of the molecule when the C≡C unsaturation is not activated. Figure 10 shows that the c-Pd/TiS catalyst provides a comparable degree of conversion to that of the Lindlar catalyst in the hydrogenation of short-chain alkynes, and is inactive when the adsorption length of the alkyne is increased to more than 8 Å. In fact, for larger alkynes, only the Lindlar catalyst provides an optimal conversion. This can be rationalized considering that the Lindlar catalyst is a two-dimensional system in which the Pb atoms create 2D isolated ensemble sites, while the HHDMA-modified catalyst is an anisotropic three-dimensional architecture in which the ligand creates hydrophobic 'pores'. These porous assemblies

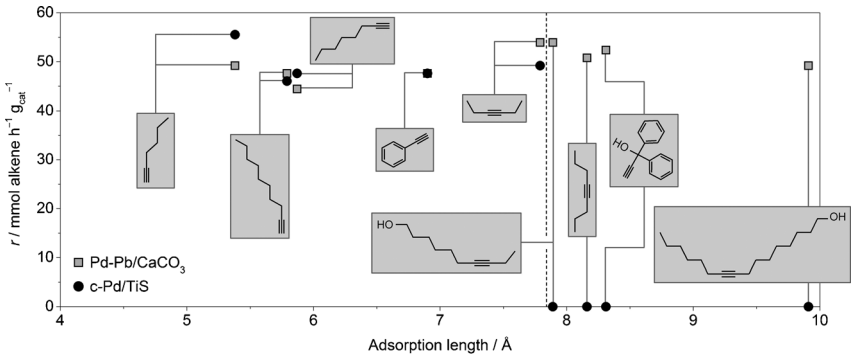

Figure 10. Influence of the adsorption length of different acetylenic compounds on the hydrogenation activity. Details on the determination of the adsorption length are given in the text and in Figure S9 in the Supporting Information. Reaction conditions: $T = 293$ K, $P = 1$ bar, $F_G(H_2) = 60$ cm^3 min^{-1}, F_L(substrate + solvent) = 3 cm^3 min^{-1}.

evolve over time (Figure S5 in the Supporting Information), allowing the acetylenic molecules to penetrate the surfactant layer (Figure 11), provided they are not too bulky. In fact, the insertion of bulky alkynes implies a penalty in terms of configurational entropy, which is compensated by the van der Waals interactions between the alkyne and the HHDMA tail. Once the acetylenic species has navigated into the surfactant layer, it needs to reorientate to be able to access the active site with the correct configuration. In this case, the adsorption can be

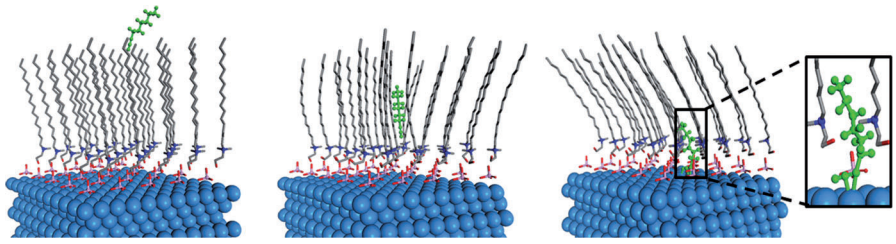

Figure 11. Proposed mechanism for the insertion and adsorption of a long-chained alkyne (represented in green) on the Pd surface of the NanoSelect™ catalyst. The picture highlights the opening of the HHDMA chains, which allows the adsorption to take place. The color codes are indicated in the captions of Figure 1 and Figure 5.

limited by the rigid distribution of the phosphate groups on the surface. Indeed, the dynamic flexibility of the ligands generates rigid elliptical cavities in close proximity to these anions, which have a maximum length of about 8 Å. Phenylacetylene does not suffer from a similar restriction not only for its small size but also because it interacts strongly with the Pd surface, opening a large ensemble. On the other hand, for 7-decyn-1-ol, 1,1-diphenyl-2-propyn-1-ol, and 9-hexadecyn-1-ol, the adsorption length is far too large to ensure that these species can interact with the palladium and react. This justifies the absence of conversion for the NanoSelect™ catalyst. These results are in agreement with the data in Figure 10. The fact that acetylenic species with adsorption lengths greater than 8 Å are not hydrogenated by the NanoSelect™ catalyst suggests that the ensemble size of Pd is constituted by approximately two adjacent palladium atoms.

In order to corroborate whether the activity of the NanoSelect™ catalyst can be enhanced with a controlled removal of the HHDMA layer, the c-Pd/TiS catalyst has been subjected to UV–ozone treatments and subsequently tested in the hydrogenation of 1-hexyne, 9-hexadecyn-1-ol, and 1-1,-diphenyl-2-propyn-1-ol (Figure S10 in the Supporting Information). The results show that the optimal duration of UV–ozone treatment is substrate specific, requiring careful fine tuning. In general, the complete removal of adsorbed HHDMA molecules is associated with a drop of the selectivity to the alkene.

Despite these findings, which limit the application of the NanoSelect™ catalyst in a broad range of industrial application (Figure 12), it is noteworthy that the catalytic systems standardly applied in industrial gas-phase catalyzed hydrogenations contain less than 0.05 wt.% Pd. On the other hand, the Lindlar catalyst applied in liquid-phase fine chemical manufacturing contains 5 wt.% Pd. In this case, the addition of Pb, in the catalyst formulation, and of quinoline, in the reaction mixture, block a large fraction of the active sites, leaving only one tenth of the Pd atoms available for hydrogenation.[15] The novel materials prepared by colloidal routes are formulated with ca. 0.5 wt.% Pd. The electrostatic interactions between the stabilizer HHDMA and the Pd nanoparticles blocks three out of four surface atoms (Figure 9), leaving single active centers that are completely isolated from the neighboring active sites. Therefore, in addition to providing a Pb-free alternative to the Lindlar catalysts, these hybrid materials competitively improve the metal utilization in liquid-phase alkyne hydrogenations by site modification and isolation.

Conclusion

We have correlated the alkyne hydrogenation performance of a representative set of Pd-based catalysts with structural descriptors derived from characterization methods, DFT calculations, and MD simulations. Supported ligand-modified palladium, developed as a lead-free alternative to the archetypal Lindlar catalyst, overcomes the suboptimal selectivity of Pd-only nanoparticles through the presence of an HHDMA capping layer. Similar to the role of lead in the Lindlar catalyst, the adsorbed ligand serves to isolate and tailor the accessibility of the active site and tune the energy landscape of the catalyst. For these reasons, in the hydrogenation of acetylenic compounds featuring isolated unsaturations and hydroxyl groups, these materials exceed the performance of the Pd–Pb alloy with a ten times lower palladium loading. Nevertheless, specific substrates, such as long-chain alkynols and alkynones, are not compatible with the use of the HHDMA-modified Pd catalysts, due to steric hindrance and acid–base interactions on the surface. This adds an extra degree of complexity in the performance of Pd nanoparticles prepared by colloidal routes. These findings provide a wide perspective on the applicability and limits of hybrid catalysts for hydrogenation, offering key insights for the design of future alkyne hydrogenation catalysts which are ultraselective to olefin production and do not suffer from accessibility constraints.

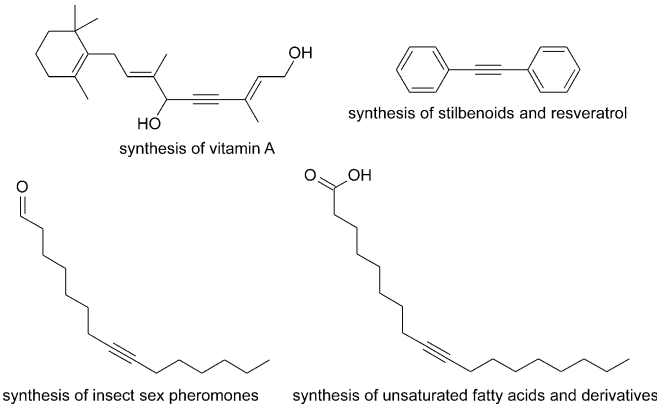

Figure 12. Important acetylenic intermediates in the pharmaceutical and fine chemical industries whose semihydrogenation is currently catalyzed by the Lindlar systems.

Experimental and Computational Section

Materials

Four supported palladium catalysts were evaluated in this study: Pd/Al_2O_3 (Sigma–Aldrich, ref: 20570-2), $Pd–Pb/CaCO_3$ (Alfa Aesar, ref: 043172), c-Pd/C (NanoSelect LF 100™, Strem Chemicals, ref:

46-1710) and c-Pd/TiS (NanoSelect LF 200™, Strem Chemicals, ref: 46-1711). The prefix 'c-' designates supported Pd catalysts which have been prepared by colloidal routes, and TiS denotes the titanium silicate support (compositional analysis has shown that the latter is characterized by a molar Ti/Si ratio of 2.3). The residual organic layer present on the surface of the Pd nanoparticles in the NanoSelect catalysts was removed by applying an UV–ozone treatment using a Bulbtronics 16 W low-pressure mercury lamp (emitting at 185 and 257 nm). The sample was positioned at a distance of 5 mm from the UV lamp for 1, 2, 5, 10, 20, 40, 60, or 120 min. The acetylenic reagents 1-pentyne (ABCR-Chemicals, 98%), 1-hexyne (Acros Organics, 98%), 3-hexyne (TCI Deutschland, 98%), 2-methyl-1-buten-3-yne (ABCR-Chemicals, 97%), 2-methyl-3-butyn-2-ol (Acros Organics, 98%), 3-methyl-1-pentyn-3-ol (TCI Deutschland, >98%), 3-methyl-1-penten-4-yn-3-ol (ABCR-Chemicals, 95%), 3-butyn-2-one (ABCR-Chemicals, 97%), 3-hexyn-2-one (ABCR-Chemicals, 97%), 1-octyne (ABCR-Chemicals, 98%), 4-octyne (ABCR-Chemicals, 99%), 9-hexadecyn-1-ol (ABCR-Chemicals, 98%), phenylacetylene (Acros Organics, 98%), 1,1-diphenyl-2-propyn-1-ol (Sigma–Aldrich, 99%), toluene (Acros Organics, 99.9%), and benzene (Sigma–Aldrich, >99.5%) were used without further purification.

Characterization

Nitrogen isotherms at 77 K were measured in a Micromeritics TriStar II instrument. Prior to measurement, the sample was degassed in vacuum at 393 K for 10 h. The palladium and lead contents in the solids were determined by inductively coupled plasma optical emission spectroscopy (ICP-OES) using a Horiba Ultra 2 instrument equipped with photomultiplier tube detection. The palladium dispersion (D) was determined by CO pulse chemisorption by using a Thermo TPDRO 1100 unit. The samples (0.05–0.1 g) were pretreated at 393 K under flowing He (20 $cm^3 min^{-1}$) for 60 min, and reduced at 348 K under flowing 5 vol.% H_2/He (20 $cm^3 min^{-1}$) for 30 min. Thereafter, 0.344 cm^3 of 1 vol.% CO/He was pulsed over the catalyst bed at 308 K every 4 min. The interval between successive pulses was minimized to avoid desorption of CO. The palladium dispersion was calculated from the amount of chemisorbed CO, considering an atomic surface density of 1.26×10^{19} atoms m^{-2} and an adsorption stoichiometry of Pd/CO = 2.[47] X-ray photoelectron spectroscopy (XPS) was performed on a VG-Microtech Multilab 3000 spectrometer featuring a hemispheric electron analyzer with 9 channeltrons and non-monochromatized $Al_{K\alpha}$ radiation at 1486.6 eV. The catalysts were pretreated at 393 K under flowing He (20 $cm^3 min^{-1}$) for 60 min, and reduced in situ at 348 K under flowing 5 vol.% H_2/He (20 $cm^3 min^{-1}$) for 30 min. The spectra were collected under ultra-high vacuum conditions (residual pressure of ca. 5×10^{-8} Pa), at a pass energy of 50 eV. All binding energies were referenced to the C 1s level at 284.6 eV in order to compensate for charging effects. The distribution and morphology of the supported palladium nanoparticles were studied by secondary electron scanning electron microscopy (SEM) and high-angle annular dark-field scanning transmission electron (HAADF-STEM) imaging, which was conducted in an FEI Magellan XHR 400 microscope using an accelerating voltage of 20 kV. The catalysts were dispersed as dry powders on holey carbon-coated copper grids. The particle size distribution was assessed by analysis of 350 individual Pd particles and the dispersion of palladium was estimated by considering particles to be truncated octahedrons with cubic symmetry and assuming the absence of an oxide shell. The N content in selected catalysts was determined by infrared spectroscopy using a LECO CHN-900 combustion furnace. Fourier transform infrared (FTIR) spectroscopy was performed in a Bruker Optics Vertex 70 spectrometer equipped with high-temperature cell, ZnSe windows, and a mercury-cadmium-telluride detector. The cell was filled with powdered catalyst and carefully leveled to minimize reflection from the sample surface. The spectra were recorded at 473 K in the range of 650–4000 cm^{-1}, by co-addition of 200 scans with a nominal resolution of 4 cm^{-1}. Thermogravimetric analysis (TGA) was performed in a Mettler Toledo TGA/DSC 1 Star system connected to a Pfeiffer Vacuum ThermoStar GSD 320 T1 Gas Analysis mass spectrometer. The analysis was performed under an air flow (40 $cm^3 min^{-1}$), ramping the temperature from 298 to 1173 K at 5 K min^{-1}. The signals of water (m/z = 18) and carbon dioxide (m/z = 44) were continuously monitored.

Catalytic tests

The hydrogenation of acetylenic compounds was carried out in a fully-automatized continuous-flow flooded-bed reactor (ThalesNano H-Cube Pro™), in which the liquid hydrocarbon and the gaseous hydrogen flow concurrently upward through a fixed bed of catalyst particles (Figure 2). Compared to the typical downward flow of a trickle-bed reactor, a flooded-bed reactor is highly advantageous for studying three-phase hydrogenation reactions since it enables improved performance by prolonging the catalyst lifetime and enhancing the heat transfer between the gas and the liquid phases.[48] The pressure drop, calculated according to the Lockhart–Martinelli correlation for a two-phase flow,[48] was insignificant (0.07 bar) along the bed and estimation of the axial dispersion corroborated minor deviations from the plug-flow regime. The contacting efficiency was within the trickle and flooded flow regimes, ensuring the absence of liquid holdup.[48] Hydrogen was generated in situ by the electrolysis of Millipore-filtered water and supplied to the reaction chamber by a mass-flow controller. The liquid feed was supplied by an HPLC pump. The reactor was equipped with a two-zone heating jacket, a pressure controller, and three thermocouples, located at the inlet, in the center, and at the outlet of the catalyst bed. In particular, during reaction, the temperature difference between these thermocouples was less than 2 K, confirming isothermal operation. The catalyst (0.1 g, particle size: 0.2–0.4 mm) was diluted and carefully mixed with silicon carbide (0.07 g, particle size: 0.2–0.4 mm) and loaded into a cartridge of approximately 30 mm length × 3.5 mm internal diameter. The influence of silicon carbide on the reactant conversion was excluded by estimation of the dilution correlation.[49] Reaction solutions contained 1 vol.% of the acetylenic substrate, toluene as the solvent, and benzene as the internal standard. The catalytic tests were performed at various temperatures (293–413 K), pressures (1–9 bar), and liquid (0.3–3 $cm^3 min^{-1}$) and H_2 flow rates (3–60 $cm^3 min^{-1}$). Importantly, under these conditions, a laminar flow is expected in both the liquid and the gas phases. The possibility of alkyne evaporation was ruled out by circulating the alkyne with the toluene solvent and the benzene internal standard for 3 h, in the absence of hydrogen, and the concentration of reactant at the reactor outlet remained constant. In addition, leaching of active Pd species from the catalyst was excluded. In fact, the liquid at the reactor outlet, containing the alkyne, alkene, toluene, and benzene, was fed to the reactor inlet (at T = 293 K, P = 1 bar, $F_G(H_2)$ = 18 $cm^3 min^{-1}$, F_L(substrate + solvent) = 0.3 $cm^3 min^{-1}$), in a cartridge filled only with diluent, and no additional hydrogenation occurred, thus evidencing no loss of the active Pd phase, in agreement with elemental analyses of the used catalysts. The reaction products were collected employing an autosampler, after reaching (in ca. 10 min) steady-state operation, and analyzed offline using a gas chromatograph (HP 6890) equipped with a HP-5 capillary column and a flame ionization detector. Helium was used as a carrier gas, flowing at 1 $cm^3 min^{-1}$. The

column was kept at an initial temperature of 303 K for 12 min and then the temperature was ramped from 303 to 473 K at 5 K min^{-1}. The conversion (X) of alkyne was determined as the amount of reacted alkyne divided by the amount of alkyne at the reactor inlet, whereas the selectivity (S) to a given alkene or alkane was quantified as the amount of that compound divided by the total amount of products.

Computational details

Quantum-mechanical calculations based on density functional theory with periodic boundary conditions were carried out with the VASP code,[50–52] using a basis set of plane waves to solve the Kohn–Sham equations, the generalized gradient approximation (GGA), and the revised Perdew–Burke–Ernzerhof (RPBE) functional.[53] The interaction between valence and core electrons was described by the projected augmented wave (PAW) method.[52] The number of plane waves was controlled by setting the cutoff energy to 450 eV. For the geometric optimization, a $5\times5\times1$ k-point mesh was used in order to sample the reciprocal space. DFT calculations focused on the Pd(111) facet, characterized by a slab with five atomic layers, which was periodically repeated in the direction perpendicular to the surface and separated by a vacuum gap of approximately 30 Å. Particularly, Pd(111) is known to be the most exposed and active surface of palladium.[6] Parallel to the surface, the supercell consisted of a primitive, $p(2\times2)$ arrangement. In the optimizations, the two atomic layers at the bottom of the slab were fixed at their bulk positions, while the upper three layers were fully relaxed. To model the Lindlar catalyst, single Pd atoms were substituted by Pb with a 0.25 monolayer coverage, considering that earlier experimental studies on the interaction of Pb with Pd in the Lindlar catalyst suggested the formation of a surface Pd_3Pb alloy.[15,54] Pd–Zn[10] and Pd–Ga[25] alloys, which are also selective catalysts for alkyne hydrogenation, were represented similarly to Pd–Pb. The crystal structure of the HHDMA ligand had been derived from the structure of hexadecyltrimethylammomium bromide.[55] This was modified using the Materials Studio software (version 6.1, Accelrys), in order to contain two units of the cationic alkyl chains in alternate configuration and two $H_2PO_4^-$ anions (Figure S4 in the Supporting Information), following the methodology described elsewhere.[56] For the adsorption of individual HHDMA molecules on palladium, van der Waals interactions were introduced with the DFT-D2 approach,[57,58] employing the parameters refined by Ruiz et al.[59] In order to investigate the flexibility of the ligand adsorbed on Pd(111), classical molecular dynamics simulations were carried out with the DL_POLY Classic code.[60] This method has been successfully employed in the past for long-time-scale simulations, which offer significantly more information on the process itself, and for large size simulations, permitting the application to macromolecular chains. However, the code cannot describe the reactivity on the surface and, thus, it is only suited to understand the ensemble size and the limitations imposed by the surfactant layer to the access of the reactants. In our case, the HHDMA–Pd system was modeled in a hexagonal simulation cell with surface dimensions of 27.5×27.5 Å^2, which is three times larger than the DFT simulation cell. The Pd surface and the HHDMA adsorbates were relaxed, keeping the $H_2PO_4^-$ ions fixed at the optimized positions provided by the DFT calculations. A combination of compatible interatomic potential models was employed for the description of the interactions between the atoms in the systems. Particularly, the generalized AMBER force field[61,62] for the HHDMA molecule and METAL[63] for palladium. This combination has been previously validated by Heinz and co-workers.[64,65] The equilibration period was 0.1 ns in the NVT ensemble. In order to fix the temperature at 273 K, the Nosé-Hoover thermostat was employed,[66,67] and the Verlet leapfrog algorithm[68] was used to integrate the equations of motion with a time step of 0.1 fs. The length of the subsequent production run for the system was 1 ns.

Acknowledgements

Financial support from ETH Zurich, the Spanish "Ministerio de Economía y Competitividad" (CTQ2012-33826), and the ICIQ Foundation is acknowledged. Dr. Yargo Bonetti and Luisa Petti (ETH Zurich) are thanked for performing UV–ozone treatments. The FIRST Laboratory and the Scientific Center for Optical and Electron Microscopy ScopeM of the Swiss Federal Institute of Technology are acknowledged for providing access to their facilities. BSC-RES is thanked for generous computational resources.

Keywords: alkynes · density functional theory · flow chemistry · hydrogenation · nanoparticles · palladium

[1] S. Nishimura, *Handbook of Heterogeneous Catalytic Hydrogenation for Organic Synthesis*, Wiley, New York, **2001**, p. 148.
[2] H. F. Rase, *Handbook of Commercial Catalysts: Heterogeneous Catalysts*, CRC Press, Boca Raton, **2000**, p. 110.
[3] Á. Molnár, A. Sárkány, M. Varga, *J. Mol. Catal. A* **2001**, *173*, 185.
[4] D. Teschner, J. Borsodi, A. Wootsch, Z. Révay, M. Hävecker, A. Knop-Gericke, S. D. Jackson, R. Schlögl, *Science* **2008**, *320*, 86.
[5] J. A. Anderson, J. Mellor, R. P. K. Wells, *J. Catal.* **2009**, *261*, 208.
[6] M. García-Mota, B. Bridier, J. Pérez-Ramírez, N. López, *J. Catal.* **2010**, *273*, 92.
[7] M. Crespo-Quesada, A. Yarulin, M. Jin, Y. Xia, L. Kiwi-Minsker, *J. Am. Chem. Soc.* **2011**, *133*, 12787.
[8] D. Mei, P. A. Sheth, M. Neurock, C. M. Smith, *J. Catal.* **2006**, *242*, 1.
[9] F. Studt, F. Abild-Pedersen, T. Bligaard, R. Z. Sørensen, C. H. Christensen, J. K. Nørskov, *Science* **2008**, *320*, 1320.
[10] F. Studt, F. Abild-Pedersen, T. Bligaard, R. Z. Sørensen, C. H. Christensen, J. K. Nørskov, *Angew. Chem.* **2008**, *120*, 9439; *Angew. Chem. Int. Ed.* **2008**, *47*, 9299.
[11] D. Teschner, Z. Révay, J. Borsodi, M. Hävecker, A. Knop-Gericke, R. Schlögl, D. Milroy, S. D. Jackson, D. Torres, P. Sautet, *Angew. Chem.* **2008**, *120*, 9414; *Angew. Chem. Int. Ed.* **2008**, *47*, 9274.
[12] D. Mei, M. Neurock, C. M. Smith, *J. Catal.* **2009**, *268*, 181.
[13] N. López, C. Vargas-Fuentes, *Chem. Commun.* **2012**, *48*, 1379.
[14] H. Lindlar, *Helv. Chim. Acta* **1952**, *35*, 446.
[15] M. García-Mota, J. Gómez-Díaz, G. Novell-Leruth, C. Vargas-Fuentes, L. Bellarosa, B. Bridier, J. Pérez-Ramírez, N. López, *Theor. Chem. Acc.* **2011**, *128*, 663.
[16] A. V. Biradar, A. A. Biradar, T. Asefa, *Langmuir* **2011**, *27*, 14408.
[17] P. Conley, R. M. Drost, M. Baffert, D. Gajan, C. Elsevier, T. W. Franks, H. Oschkinat, L. Veyre, A. Zagdoun, A. Rossini, M. Lelli, A. Lesage, G. Casano, O. Ouari, P. Tordo, L. Emsley, C. Copéret, C. Thieuleux, *Chem. Eur. J.* **2013**, *19*, 12234.
[18] S. Domínguez-Domínguez, Á. Berenguer-Murcia, B. K. Pradhan, Á. Linares-Solano, D. Cazorla-Amorós, *J. Phys. Chem. C* **2008**, *112*, 3827.
[19] W. Long, N. A. Brunelli, S. A. Didas, E. W. Ping, C. W. Jones, *ACS Catal.* **2013**, *3*, 1700.
[20] Y. Yabe, Y. Sawama, Y. Monguchi, H. Sajiki, *Catal. Sci. Technol.* **2014**, *4*, 260.
[21] Y. Segura, N. López, J. Pérez-Ramírez, *J. Catal.* **2007**, *247*, 383.
[22] B. Bridier, N. López, J. Pérez-Ramírez, *Dalton Trans.* **2010**, *39*, 8412.
[23] G. Vilé, B. Bridier, J. Wichert, J. Pérez-Ramírez, *Angew. Chem.* **2012**, *124*, 8748; *Angew. Chem. Int. Ed.* **2012**, *51*, 8620.
[24] G. Vilé, D. Baudouin, I. N. Remediakis, C. Copéret, N. López, J. Pérez-Ramírez, *ChemCatChem* **2013**, *5*, 3750.

[25] G. Wowsnick, D. Teschner, M. Armbrüster, I. Kasatkin, F. Girgsdies, Y. Grin, R. Schlögl, M. Behrens, *J. Catal.* **2014**, *309*, 221.
[26] B. Bridier, J. Pérez-Ramírez, *J. Am. Chem. Soc.* **2010**, *132*, 4321.
[27] J. P. Boitiaux, J. Cosyns, S. Vasudevan, *Appl. Catal.* **1983**, *6*, 41.
[28] A. Roucoux, J. Schulz, H. Patin, *Chem. Rev.* **2002**, *102*, 3757.
[29] C. Burda, X. Chen, R. Narayanan, M. A. El-Sayed, *Chem. Rev.* **2005**, *105*, 1025.
[30] N. Semagina, L. Kiwi-Minsker, *Catal. Rev. Sci. Eng.* **2009**, *51*, 147.
[31] N. Semagina, L. Kiwi-Minsker, *Catal. Lett.* **2009**, *127*, 334.
[32] R. Venkatesan, M. H. G. Prechtl, J. D. Scholten, R. P. Pezzi, G. Machado, J. Dupont, *J. Mater. Chem.* **2011**, *21*, 3030.
[33] H. Bönnemann, W. Brijoux, R. Brinkmann, E. Dinjus, T. Joussen, B. Korall, *Angew. Chem.* **1991**, *103*, 1344; *Angew. Chem. Int. Ed. Engl.* **1991**, *30*, 1312.
[34] M. Crespo-Quesada, J. M. Andanson, A. Yarulin, B. Lim, Y. Xia, L. Kiwi-Minsker, *Langmuir* **2011**, *27*, 7909.
[35] P. T. Witte, P. H. Berben, S. Boland, E. H. Boymans, D. Vogt, J. W. Geus, J. G. Donkervoort, *Top. Catal.* **2012**, *55*, 505.
[36] P. T. Witte, S. Boland, F. Kirby, R. van Maanen, B. F. Bleeker, D. A. M. de Winter, J. A. Post, J. W. Geus, P. H. Berben, *ChemCatChem* **2013**, *5*, 582.
[37] Y. Zhao, L. Jia, J. A. Medrano, J. R. H. Ross, L. Lefferts, *ACS Catal.* **2013**, *3*, 2341.
[38] M. Irfan, T. N. Glasnov, C. O. Kappe, *ChemSusChem* **2011**, *4*, 300.
[39] M. A. G. Hevia, B. Bridier, J. Pérez-Ramírez, *Appl. Catal. A* **2012**, *439–440*, 163.
[40] R. Schlögl, K. Noack, H. Zbinden, A. Reller, *Helv. Chim. Acta* **1987**, *70*, 3.
[41] D. Briggs, M. P. Seah, *Practical Surface Analysis by Auger and X-ray Photoelectron Spectroscopy*, 1st ed., Wiley, Chichester, **1983**, p. 26.
[42] B. H. Stuart, *Infrared Spectroscopy - Fundamentals and Applications*, Wiley, Chichester, **2004**, p. 45.
[43] X. Yang, N. Yan, Z. Fei, M. Crespo-Quesada, G. Laurenczy, L. Kiwi-Minsker, Y. Kou, Y. Li, P. Dyson, *Inorg. Chem.* **2008**, *47*, 7444.
[44] O. M. Magnussen, *Chem. Rev.* **2002**, *102*, 679.
[45] B. Bridier, D. Karhánek, J. Pérez-Ramírez, N. López, *ChemCatChem* **2012**, *4*, 1420.
[46] N. Mehio, S. Dai, D. Jiang, *J. Phys. Chem. A* **2014**, *118*, 1150.
[47] G. Fagherazzi, P. Canton, P. Riello, N. Pernicone, F. Pinna, M. Battagliarin, *Langmuir* **2000**, *16*, 4539.
[48] C. N. Satterfield, *AIChE J.* **1975**, *21*, 209.
[49] R. J. Berger, J. Pérez-Ramírez, F. Kapteijn, J. A. Moulijn, *Chem. Eng. J.* **2002**, *90*, 173.
[50] G. Kresse, J. Furthmuller, *Phys. Rev. B* **1996**, *54*, 11169.
[51] G. Kresse, J. Furthmuller, *Comput. Mater. Sci.* **1996**, *6*, 15.
[52] G. Kresse, D. Joubert, *Phys. Rev. B* **1999**, *59*, 1758.
[53] B. Hammer, L. B. Hansen, J. K. Nørskov, *Phys. Rev. B* **1999**, *59*, 7413.
[54] D. Chadwick, M. A. Karolewski, *Surf. Sci.* **1983**, *126*, 41.
[55] Z. B. Wei, X. L. Wei, X. H. Wang, Z. N. Wang, J. Liu, *J. Mater. Chem.* **2011**, *21*, 6875.
[56] N. Almora-Barrios, G. Novell-Leruth, P. Whiting, L. M. Liz-Marzán, N. López, *Nano Lett.* **2014**, *14*, 871.
[57] S. Grimme, *J. Comput. Chem.* **2006**, *27*, 1787.
[58] T. Bucko, J. Hafner, S. Lebegue, J. G. Angyan, *J. Phys. Chem. A* **2010**, *114*, 11814.
[59] V. G. Ruiz, W. Liu, E. Zojer, M. Scheffler, A. Tkatchenko, *Phys. Rev. Lett.* **2012**, *108*, 146103.
[60] I. T. Todorov, W. Smith, K. Trachenko, M. T. Dove, *J. Mater. Chem.* **2006**, *16*, 1911.
[61] W. D. Cornell, P. Cieplak, C. I. Bayly, I. R. Gould, K. M. Merz, D. M. Ferguson, D. C. Spellmeyer, T. Fox, J. W. Caldwell, P. A. Kollman, *J. Am. Chem. Soc.* **1995**, *117*, 5179.
[62] J. M. Wang, P. Cieplak, P. A. Kollman, *J. Comput. Chem.* **2000**, *21*, 1049.
[63] H. Heinz, R. A. Vaia, B. L. Farmer, R. R. Naik, *J. Phys. Chem. C* **2008**, *112*, 17281.
[64] J. Feng, J. M. Slocik, M. Sarikaya, R. R. Naik, B. L. Farmer, H. Heinz, *Small* **2012**, *8*, 1049.
[65] J. Feng, R. B. Pandey, R. J. Berry, J. M. Slocik, R. R. Naik, B. L. Farmer, H. Heinz, *Soft Matter* **2011**, *7*, 2113.
[66] S. Nosé, *J. Chem. Phys.* **1984**, *81*, 511.
[67] W. G. Hoover, *Phys. Rev. A* **1985**, *31*, 1695.
[68] L. Verlet, *Phys. Rev.* **1967**, *159*, 98.

Received: December 6, 2013
Published online on April 17, 2014